

Journal Pre-proof

A deep learning network for classifying arteries and veins in montaged wide-field OCT angiograms

Min Gao, Yukun Guo, Tristan T. Hormel, Kotaro Tsuboi, George Pacheco, David Poole, Steven T. Bailey, Christina J. Flaxel, David Huang, Thomas S. Hwang, Yali Jia



PII: S2666-9145(22)00038-0

DOI: <https://doi.org/10.1016/j.xops.2022.100149>

Reference: XOPS 100149

To appear in: *Ophthalmology Science*

Received Date: 11 October 2021

Revised Date: 16 March 2022

Accepted Date: 28 March 2022

Please cite this article as: Gao M., Guo Y., Hormel T.T., Tsuboi K., Pacheco G., Poole D., Bailey S.T., Flaxel C.J., Huang D., Hwang T.S. & Jia Y., A deep learning network for classifying arteries and veins in montaged wide-field OCT angiograms, *Ophthalmology Science* (2022), doi: <https://doi.org/10.1016/j.xops.2022.100149>.

This is a PDF file of an article that has undergone enhancements after acceptance, such as the addition of a cover page and metadata, and formatting for readability, but it is not yet the definitive version of record. This version will undergo additional copyediting, typesetting and review before it is published in its final form, but we are providing this version to give early visibility of the article. Please note that, during the production process, errors may be discovered which could affect the content, and all legal disclaimers that apply to the journal pertain.

© 2022 Published by Elsevier Inc. on behalf of American Academy of Ophthalmology.

1 Title

2 A deep learning network for classifying arteries and veins in montaged wide-field OCT angiograms

3 Authors

4 Min Gao¹, Yukun Guo¹, Tristan T. Hormel¹, Kotaro Tsuboi¹, George Pacheco¹, David Poole¹, Steven T.
5 Bailey¹, Christina J. Flaxel¹, David Huang¹, Thomas S. Hwang¹, and Yali Jia^{1,2}

6 1 Casey Eye Institute, Oregon Health & Science University, Portland, OR 97239, USA

7 2 Department of Biomedical Engineering, Oregon Health & Science University, Portland, OR 97239,
8 USA
9

10 **Key Words:** Deep learning; classification of arteries and veins; measurement of their caliber and
11 tortuosity

12 Abbreviations and Acronyms:

13 **OCT** = optical coherence tomography; **OCTA** = optical coherence tomographic angiography; **DR** =
14 diabetic retinopathy; **BRVO** = branch retinal vein occlusion; **SSADA** = split-spectrum amplitude-
15 decorrelation angiography; **ILM** = internal limiting membrane; **OPL** = outer plexiform layer; **CE** =
16 categorical cross-entropy; **PDR** = proliferative diabetic retinopathy; **NPDR** = non-proliferative diabetic
17 retinopathy; **RVO** = Retinal venous occlusion; **IoU** = Intersection over Union; **CAVnet** = classification
18 of artery and vein network

19 Corresponding Author:

20 Yali Jia, Ph.D. jiaya@ohsu.edu

21 Casey Eye Institute, Oregon Health & Science University, 515 SW Campus Dr., Portland, OR 97239.

22 Financial Support:

23 National Institutes of Health (R01 EY027833, R01 EY024544, R01 EY031394, P30 EY010572, T32
24 EY023211);

25 Unrestricted Departmental Funding Grant and William & Mary Greve Special Scholar Award from
26 Research to Prevent Blindness (New York, NY);

27 Bright Focus Foundation (G2020168).

28 Conflict of interest:

29 Oregon Health & Science University (OHSU), Yali Jia and David Huang have a financial interest in
30 Optovue, Inc., a company that may have a commercial interest in the results of this research and
31 technology. These potential conflicts of interest have been reviewed and are managed by OHSU. The
32 other authors do not report any potential financial conflicts of interest.

33 **ABSTRACT**

34 **Purpose:** To propose a deep-learning-based method to differentiate arteries from veins in montaged
 35 wide-field optical coherence tomography (OCT) angiograms.

36 **Design:** Cross-sectional study.

37 **Participants:** A total of 232 participants including 109 participants with diabetic retinopathy (DR), 64
 38 participants with branch retinal vein occlusion (BRVO), 27 participants with diabetes but without DR,
 39 and 32 healthy participants.

40 **Methods:** We propose a convolutional neural network (CAVnet) to classify retinal blood vessels on
 41 montaged wide-field optical coherence tomographic angiography (OCTA) *en face* images as arteries and
 42 veins. 235 retinal angiograms from 88 eyes were used to train CAVnet, and 302 retinal angiograms from
 43 144 eyes were used for testing. This method takes the OCTA images as input and outputs the
 44 segmentation results with arteries and veins down to the level of precapillary arterioles and postcapillary
 45 venules. The network also identifies their intersections. We evaluated the agreement (in pixels) between
 46 segmentation results and the manually graded ground truth using sensitivity, specificity, F1-score,
 47 and Intersection over Union (IoU). Measurements of arterial and venous caliber or tortuosity are made on
 48 our algorithm's output of healthy and diseased eyes.

49 **Main Outcome Measures:** Classification of arteries and veins, arterial and venous caliber, arterial and
 50 venous tortuosity.

51 **Results:** For classification and identification of arteries, the algorithm achieved average sensitivity of
 52 95.3%, specificity of 99.6%, F1 score of 94.2%, and IoU of 89.3%. For veins, the algorithm achieved
 53 average sensitivity of 94.4%, specificity of 99.7%, F1 score of 94.1%, and IoU of 89.2%. We also
 54 achieved an average sensitivity of 76.3% in identifying intersection points. The results show CAVnet has
 55 high accuracy on differentiating arteries and veins in DR and BRVO cases. These classification results are
 56 robust across two instruments and multiple scan volume sizes. CAVnet's outputs were used to measure
 57 arterial and venous caliber or tortuosity, and pixel-wise caliber and tortuosity maps were generated.
 58 Differences between healthy and diseased eyes were demonstrated, indicating potential clinical utility.

59 **Conclusions:** CAVnet can classify artery and vein and their branches with high accuracy, and is
 60 potentially useful in the analysis of vessel type-specific features on diseases such as branch retinal artery
 61 occlusion and branch retinal vein occlusion.

63 **1. Introduction**

64 Optical coherence tomographic angiography (OCTA) is a powerful imaging modality for noninvasive, 3-
 65 dimensional and detailed assessment of retinal vasculature^{1,2}. Numerous studies have demonstrated the
 66 utility of OCTA in retinal diseases. For example, nonperfusion area is a key biomarker in the evaluation
 67 of diabetic retinopathy (DR)³⁻⁶, and accurate identification and segmentation of choroidal
 68 neovascularization in outer retinal angiogram is helpful for the diagnosis and management of neovascular
 69 age-related macular degeneration⁷.

70 One challenge with OCTA technology is distinguishing arteries from veins. Correctly identifying
 71 the vessels can be critical in understanding certain diseases. For example, retinal arteriolar narrowing is
 72 associated with hypertension and diabetic retinopathy^{8,9}; venous beading is a feature of moderate to
 73 severe DR¹⁰; different types of retinal vascular occlusion (artery or vein) would have vessel-specific
 74 dilation or constriction^{11,12}. Classifying arteries and veins may enable improved disease characterization
 75 by specifically evaluating the vessel for pathologic changes. However, manual segmentation of arteries
 76 and veins not only requires specific expertise but is also time-consuming. Automation of this task is
 77 indispensable if specific characterization for arteries and veins is to be practical.

78 A number of algorithms have been proposed to classify arteries and veins using OCTA. However,
 79 limitations in each approach still call for improvement. Alam et al. proposed using fundus photograph or
 80 structural optical coherence tomography (OCT) features to guide the classification of arteries and veins in
 81 OCTA images^{13,14}. These algorithms based on OCTA need other imaging modalities or structural OCT to
 82 help classify arteries and veins, which in turn may introduce more errors by fusing multiple types of
 83 images. Xu et al. differentiated veins from arteries in OCTA by identifying deep capillary plexus
 84 vortices¹⁵. Although they described a method for distinguishing retinal arteries from veins on OCTA, it is
 85 not an automated approach. Ishibazawa et al. evaluated the accuracy and reliability in differentiating
 86 retinal arteries from veins using wide-field OCTA¹⁶. While their study showed that readers can correctly
 87 classify large arteries and veins using only wide-field OCTA in healthy eyes and eyes with severe DR,
 88 trained graders were required for the task. Kim et al. proposed to differentiate arteries from veins in OCT
 89 and OCTA of the mouse retina and their method manually performed artery and vein classification using
 90 vascular morphology and blood flow signatures¹⁷. This means the approach will not scale well for clinical
 91 application.

92 More recently, deep learning has been used to aid OCTA image enhancement and segmentation of
 93 vascular features¹⁸. Alam et al. also proposed a deep learning approach to artery/vein classification on
 94 OCTA¹⁹. However, their approach focused on just the macular region and required structural OCT input,

95 which increased computation requirements. Furthermore, the requirement for structural OCT input means
 96 that graders should review structural information as well as angiographic if a scan requires verification,
 97 increasing the amount of time needed to determine if correction is required. Their results also include a
 98 significant number of anatomically inaccurate spurs where vessel walls should be smooth.

99 Here, we propose an end-to-end convolutional neural network, CAVnet (Classification of Artery and
 100 Vein Network), that can classify arteries and veins in montaged wide-field OCT angiograms covering a
 101 6×17-mm field of view as well as subimages in the same area. In this algorithm, the classification is
 102 purely based on OCTA input, and the vessel types are stratified starting from peripapillary major retinal
 103 arteries/veins to precapillary branches. In this study, we also characterize the caliber and tortuosity of
 104 arteries and veins of healthy and eyes with retinopathy.

105 **2. Methods**

106 **2.1 Data acquisition**

107 The study was approved by an Institutional Review Board/Ethics Committee of Oregon Health & Science
 108 University, and informed consent was collected from all participants, in compliance with the Declaration
 109 of Helsinki. In this study, 27 healthy controls, 27 eyes from diabetic eyes without DR, and 109
 110 participants diagnosed with DR (52 mild to moderate non-proliferative diabetic retinopathy (NPDR), 57
 111 severe NPDR and proliferative diabetic retinopathy (PDR)), and 64 participants diagnosed with branch
 112 retinal vein occlusion (BRVO) were enrolled. One eye from each participant underwent 6×6-mm
 113 volumetric scans centered at the macula and the immediate areas nasal and temporal to the macular scan
 114 using a 70-kHz AngioVue™ OCTA system (RTVue-XR Avanti; Optovue, Inc.) with a central
 115 wavelength of 840 nm. In this scan pattern, two repeated B-scans were obtained at each of 400 raster
 116 positions and each B-scan containing 400 A-lines. Additionally, five healthy eyes were scanned using a
 117 120-kHz AngioVue OCTA system (Solix, Optovue, Inc.). The eyes were scanned using 9×9-mm scan
 118 patterns. The details of the acquired data are presented in Table 1. Two repeated B-scans were taken at
 119 each of the 600 raster positions, and each B-scan consisted of 600 A-lines. The split-spectrum amplitude-
 120 decorrelation angiography (SSADA) algorithm was used to generate the OCTA data from both
 121 instruments¹. Retinal layer boundaries were segmented by a guided bidirectional graph search algorithm²⁰.
 122 Inner retinal angiograms were generated by maximum projection of the OCTA signal in a slab from
 123 internal limiting membrane (ILM) to outer plexiform layer (OPL).

124 **2.2. Convolutional neural network architecture**

125 The structure of CAVnet is illustrated in Fig.1. *En face* OCT angiograms projected from the retina were
 126 input to the network to segment arteries and veins. CAVnet adopted a U-net-like architecture that is
 127 comprised of an encoder and a decoder. The encoder includes four down-sampling layers to reduce the
 128 image resolution and five sub-modules to extract features at different scales. Each sub-module fused
 129 features extracted by a convolution layer and atrous convolutional layer with different receptive fields.
 130 The features with different receptive fields and at different scales provide the network with contextual and
 131 global information. The decoder consists of four sub-modules and deconvolutional upsampling layers.
 132 The resolution is sequentially increased through the up-sampling operation until it is consistent with the
 133 resolution of the input image. The network also uses a skip connection to connect the up-sampling result
 134 with the output of the sub-module with the same resolution in the encoder as the input of the next sub-
 135 module in the decoder. Except for the last convolutional layer, batch normalization and a LeakyRelu
 136 activation function are used after each convolutional layer. A softmax activation function is used for
 137 multiple classifications in the last convolutional layer.

138 **2.3. Training**

139 **2.3.1. Subjects and ground truth generation**

140 The datasets included the retinal angiograms of eyes without DR (either healthy or diabetes mellitus
 141 without DR), eyes from patients with DR, and eyes with BRVO. For each eye without DR and eye with
 142 DR, volumetric OCT and OCTA scans from the nasal, macula, and temporal were acquired. For each eye
 143 with BRVO, volumetric OCT and OCTA scans from the macula were collected. 29 scans with poor
 144 quality were excluded, yielding a total of 537 retinal angiograms. 235 angiograms from 88 eyes were used
 145 for training, and 302 angiograms from 144 eyes were used for testing, no eyes were shared in training and
 146 testing of the model; the numbers of eyes are shown in Table 1. In order to make a reliable and accurate
 147 quantitative comparison of the test results, we set the number of eyes from DR with different severity to
 148 be the same in the test dataset. In the training phase, the angiograms from three regions were fed into
 149 CAVnet, separately. For predictions, the input can be either independent angiograms from these three
 150 regions or wide-field angiograms, which include nasal, macular, or temporal scans. Even though a
 151 previous study has confirmed that *en face* OCTA allows for accurate and reliable artery and vein
 152 identification¹⁶, we still used fundus photographs as a guide to delineate accurate ground truth for training.
 153 First, we enhanced the OCT angiogram quality using a deep-learning-based capillary reconstruction
 154 algorithm²¹ [Fig.2 (B)], which is only used for ground truth delineating. Then two certified graders (G.P.;
 155 D.P.) manually delineated arteries and veins on enhanced OCTA images according to the corresponding
 156 fundus photographs [Fig.2 (D, E)]. The third certified grader (M.G.) reviewed and corrected the
 157 delineated ground truth maps. In color fundus photographs and OCTA [Fig.2 (A, D, E)], various

158 characteristics can help to differentiate arteries from veins: 1) arteries have higher reflectance than veins;
 159 2) the central light reflex is wider in arteries and smaller in veins; 3) arteries are smaller-caliber than
 160 adjacent veins; 4) normally, arteries and veins alternate as each vein drains the capillary bed perfused by
 161 adjacent arteries^{15,22}; 5) arteries do not cross other arteries and veins do not cross other veins¹⁶. 6) there
 162 are obviously capillary-free zones near the retinal arteries in OCTA images^{23,24}; These properties provide
 163 graders with sufficient information to accurately delineate the ground truth.

164 **2.3.2. Training parameters**

165 During training, we used a combination of dice and categorical cross-entropy loss as the loss function.
 166 The dice coefficient D is used to measure the overlap of the two segmentations

$$167 D = \frac{2|Y \cap Y'|}{|Y| + |Y'|} \quad (1)$$

168 where Y is the ground truth and Y' is the predicted image, $|Y \cap Y'|$ is the cardinality of intersection of the Y
 169 and Y' , and $|Y|$ and $|Y'|$ represent the number of elements in Y and Y' , respectively. D is a value between
 170 0 and 1, and with 0 indicating no overlap and 1 a perfect overlap.

171 The categorical cross-entropy loss

$$172 CE = -\sum_i y_i \log y'_i \quad (2)$$

173 is usually used for multiple classifications²⁵, where y_i is the ground truth of the i^{th} category. y'_i is the
 174 output results of the i^{th} category. CE is a value between 0 and positive infinity, and close to 0 when the
 175 predicted image is approaching the ground truth. The loss function is then defined as:

$$176 L = (1 - D) + CE. \quad (3)$$

177 The combination of dice loss and categorical cross-entropy helped with category imbalance in the training
 178 data²⁶.

179 We used 400×400-pixel 6×6-mm images to train CAVnet. Several data augmentation methods were
 180 used to expand the training dataset: each batch of images is randomly flipped horizontally, vertically, and
 181 transposed before being fed into the network for iterative training. Considering both convergence time
 182 and hardware limitations, the training batch size was set to 2. We used an Adam optimizer²⁷ with an
 183 initial learning rate of 0.001 to optimize the loss. The learning rate was reduced by a factor of 0.1 when
 184 the loss didn't decline after 10 epochs. The minimum learning rate is 1×10^{-8} . When the loss does not
 185 change more than 1×10^{-5} in 20 epochs, training will stop. CAVnet was implemented using Python 3.7
 186 with Keras (Tensorflow-backend) on a PC with a 64G RAM and Intel i7 CPU, and 2 NVIDIA GeForce

187 GTX1080Ti graphics cards. For more details of hyper-parameter settings, please refer to
 188 <https://github.com/octangio/CAVnet>.

189 **3. Results**

190 **3.1 Performance evaluation**

191 To assess the performance of our algorithm, we separately evaluated arteries, veins, and intersection point
 192 accuracy on the test dataset. The pixel-wise sensitivity (Eq. (4)), specificity (Eq. (5)), F1 score (Eq. (6)),
 193 and intersection-over-union (IoU) (Eq. (7)) between the segmentation results and the ground truth were
 194 evaluated as follows:

$$195 \quad \text{Sensitivity} = \frac{\text{TP}}{\text{TP} + \text{FN}} \quad (4)$$

$$196 \quad \text{Specificity} = \frac{\text{TN}}{\text{TN} + \text{FP}} \quad (5)$$

$$197 \quad \text{F1-score} = \frac{2 \times \text{TP}}{2 \times \text{TP} + \text{FP} + \text{FN}} \quad (6)$$

$$198 \quad \text{IoU} = \frac{\text{TP}}{\text{TP} + \text{FP} + \text{FN}} \quad (7)$$

199 Where TP is true positive, TN is true negative, FN is false negative, FP is false positive. Our algorithm
 200 achieved high performance with each of these metrics for artery and vein classification (Table 2), but
 201 artery/vein intersection points were only partially accurate. For determining whether intersection points
 202 output by the network are the ones manually graded, we dilated the network output using a 3×3 disk-
 203 shaped structuring element. This helps to define the match between output and ground truth by
 204 confirming the location correlation. We speculate on this performance gap in the discussion.

205 For qualitative verification of these results, we montaged nasal, macular, and temporal angiograms
 206 into a wide-field angiogram covering a 6×17 -mm field of view [Fig.3]. The predicted results are highly
 207 consistent with the ground truth whether on healthy eyes [Fig.3 (A1-A3)] or on eyes with DR [Fig.3 (B1-
 208 B3)]. As the image shows, CAVnet classified arteries and veins down to the level of precapillary
 209 arterioles and postcapillary venules.

210 CAVnet may misclassify part of an artery to a vein or vice versa [Fig.4 (A, B)] when some features
 211 are ambiguous. Other potentially troublesome regions include artery-vein-intersections [Fig.4 (C, D)].

212 **3.2 Caliber of arteries and veins**

213 We calculated the caliber of arteries and veins on the test dataset using CAVnet's output. The caliber of
 214 the blood vessels was defined as the ratio of vascular area and vascular length that were acquired from a
 215 binarized and skeletonized artery-vein OCTA map, respectively. To calculate vessel caliber, we consider

each foreground pixel as well as the 7 adjoining pixels along the skeletonized artery-vein OCTA map in each direction (15 pixels total) and calculate the ratio of the vessel area to the vessel length. Then the caliber value was mapped to the binarized artery-vein OCTA map [Fig.5 (A-C)]. The caliber was calculated in the 6×6-mm angiograms excluding a 2-mm diameter circle centered on the optic disc. Caliber changes can be observed on the caliber map of angiograms in Fig.5 (A-C). The minimal caliber that CAVnet can detect is 1 pixel (15 μm). For statistical analysis of these results, we treated each eye as a single observation. We performed the Kolmogorov-Smirnov test, which indicated that neither the arterial nor venous caliber in nasal, macular, and temporal areas was normally distributed. For each area, a nonparametric Kruskal-Wallis test was applied to suggest if there is a difference between at least one pair of groups. Then, to find out which pairs of groups have a difference, post-hoc tests with Bonferroni correction were performed on each pair of groups. We found that there is no significant difference in the arterial caliber between eyes without DR and eyes with mild to moderate non-proliferative diabetic retinopathy (NPDR) in the three areas [Fig.5 (D)] (nasal, $P=1.00$; macula, $P=0.99$; temporal, $P=1.00$); however, compared to eyes without DR or eyes with mild to moderate NPDR, the arterial caliber of eyes with either severe NPDR or PDR was significantly reduced [Fig.5 (D)]. There is no significant difference in venous caliber between eyes without DR and eyes with DR in the optic disc area ($P=0.34$, Kruskal-Wallis test). Compared to eyes without DR, venous caliber in eyes with mild to moderate NPDR had no significant difference in the macular ($P=0.24$) and temporal ($P=1.00$) areas; however, venous caliber in eyes with either severe NPDR or PDR was smaller in the macular region ($P=0.003$) [Fig.5 (E)]. Compared to eyes with mild to moderate NPDR, venous caliber in eyes with either severe NPDR or PDR was also greatly reduced in the temporal area ($P=0.01$) [Fig.5 (E)]. We also used a Mann-Whitney U test to compare the caliber of arteries and veins in 17 healthy eyes from test dataset. The caliber of arteries (mean \pm standard deviation, $69.6 \pm 25.3 \mu\text{m}$) is much smaller than that of veins ($82.6 \pm 31.0 \mu\text{m}$) ($P=0.003$) at the nasal location. Arterial ($48.2 \pm 2.2 \mu\text{m}$) and venous ($51.3 \pm 3.5 \mu\text{m}$) caliber ($P=0.006$) is also different at temporal locations [Fig.6 (B)], but this difference disappears in the macula ($P=0.92$). In addition, we calculated the caliber of major peripapillary arteries and veins (radiated from optic nerve head) in the nasal scans [Fig.7]. The caliber of the major veins ($113.7 \pm 20.2 \mu\text{m}$) is much larger than that of the major arteries ($100.2 \pm 16.1 \mu\text{m}$, $P=0.001$, Mann-Whitney U test). This result corresponds to the previous findings- i.e. that major vein caliber ($120.9 \pm 27.2 \mu\text{m}$) is much larger than that of the major arteries ($103.3 \pm 22.2 \mu\text{m}$, $P<0.001$)- by Falavarjani et al. using a manual measurement method²⁸.

246 3.3 Tortuosity

247 We also calculated the tortuosity of arteries and veins using CAVnet's output. For each foreground pixel
 248 in the skeletonized artery-vein map, we use the 100 adjoining pixels to either side (201 pixels total) to
 249 calculate the tortuosity. The tortuosity value was mapped to the binarized artery-vein OCTA map [Fig.8

250 (A, B, C)]. The tortuosity was calculated in the 6×6-mm angiograms excluding a 2-mm diameter circle
 251 centered on the optic disc. We adopted the same statistic test method from the last section for tortuosity
 252 comparisons. Although vessels with large tortuosity values were highlighted in the maps, the tortuosity
 253 had no significant changes in eyes with mild to moderate NPDR compared to eyes without DR for either
 254 arteries or veins [Fig.8 (D, E)]. Compared to eyes without DR or eyes with mild to moderate NPDR, the
 255 mean tortuosity also had no significant changes in eyes with either severe NPDR or PDR [Fig.8 (D, E)].
 256 No significant difference was found in the mean tortuosity of arteries compared to veins at nasal, macular,
 257 or temporal locations in healthy eyes [Fig.9], which is consistent with previous measurements²⁹.

258 **3.4 Performance on scans from eyes with other retinal vascular diseases**

259 Retinal venous occlusion (RVO) is the second most common retinal vascular disease after diabetic
 260 retinopathy³⁰, and is a disease that shows different pathology on arteries and veins, respectively. We
 261 applied our algorithm to macular scans from 64 eyes with branch retinal vein occlusion (BRVO) [Fig.10
 262 (A1)]. We also calculated performance metrics such as sensitivity or F1 score for CAVnet's output on
 263 these data. The results showed high classification accuracy on these eyes [Fig.10 (B1)] (Table 3). We also
 264 calculated vessel caliber [Fig.10 (C1)] and the tortuosity [Fig.10 (D1)] for this data set. Results from 17
 265 healthy eyes from the test dataset and 64 eyes with BRVO in the macular center area showed that the
 266 caliber of arteries and veins in eyes with BRVO both greatly reduced compared to healthy eyes ($P<0.001$,
 267 Mann-Whitney U test) [Fig.11 (A)]. A previous study using revised Parr-Hubbard formulas also showed
 268 that there were significant differences in mean central retinal arterial diameter and venous diameter
 269 between the control group and the BRVO group ($P < 0.05$)³¹. The tortuosity of veins significantly
 270 increased ($P<0.001$, Mann-Whitney U test), and the tortuosity of arteries had no significant change
 271 ($P=0.18$, Mann-Whitney U test) [Fig.11 (B)], which is consistent with previously reported work showing
 272 increased venous tortuosity in eyes with BRVO by observing the number of tortuous vessels³².

273 **3.5 Performance on scans from different devices and larger-field-of-view scans**

274 In addition to testing data from an AngioVue device, we also tested our algorithm on larger-field-of-view
 275 9×9-mm angiograms from a Solix instrument [Fig.12]. The predicted artery and vein maps also appear to
 276 be correct, indicating performance did not noticeably degrade on different devices (Table 4).

277 **4. Discussion**

278 The U-Net is a popular architecture developed for biomedical image segmentation that can learn to
 279 segment features using relatively small datasets while maintaining feature resolution through the use of
 280 skip connections. There are many applications of U-Nets in biomedical image segmentation, which show
 281 reliable and highly accurate results^{33,34}. A U-net-like architecture we adopted in this study is an end-to-

282 end fully convolutional network that includes an encoder and a decoder. CAVnet can automatically and
 283 accurately classify arteries and veins montaged wide-field OCT angiograms, and includes several
 284 innovations. Among these advantages is the input data set. While arteries and veins can be distinguished
 285 by morphologic (i.e., caliber) and anatomic (i.e., the alternating artery-vein rule) features available in
 286 OCTA images, such an identification is often difficult and therefore time-consuming for human graders.
 287 For this reason, artery/vein differentiation in OCTA images has usually been supplemented with other
 288 imaging modalities, for example, oximetry^{13,35}. However, combinations of multiple imaging modalities
 289 introduce a large burden into clinical practice, and so should be avoided if a result can be achieved using
 290 just a single imaging technique. Our network achieves artery/vein differentiation using only a single OCT
 291 angiogram as input.

292 For prediction, the input to CAVnet could be independent angiograms from nasal, macular, and
 293 temporal regions, which can save computing budget. Wide-field images can also function as input. Post-
 294 processing on the CAVnet output can also stratify vessels with caliber ranging from major peripapillary
 295 vessels (~225 um) to pericapillary levels (~15 um). By identifying vessels at multiple orders and scales,
 296 CAVnet can provide more comprehensive information concerning retinal circulation, which could be
 297 helpful for assessing disease. Lastly, we believe that artery/vein classification is broadly useful for OCTA
 298 image analysis. Since arteries and veins are not routinely differentiated, disparate effects on each by
 299 various diseases may go undetected, even though such information could be used to improve diagnosis.
 300 Furthermore, from a basic research perspective, artery/vein classification could aid investigations of
 301 pathophysiology.

302 We used several metrics to assess the algorithm's performance, including sensitivity, specificity, F1-
 303 score, and intersection-over-union. We found that our network performed strongly in each of these
 304 categories, with each of sensitivity, specificity, and F1-score approaching or exceeding 95% accuracy.
 305 Performance gauged by intersection-over-union was slightly lower (~90% accuracy), but some of the
 306 inaccuracy in this metric may represent anatomically meaningless disparities resulting from single-pixel
 307 width translocations between the ground truth and the network output. In each case, performance was
 308 essentially equivalent for performing artery or vein segmentation, indicating no bias toward one vessel
 309 type or the other in output. We also investigated network applicability by characterizing CAVnet's output
 310 on different image sizes, noting no obvious performance drop off³⁶. Moreover, our results did not
 311 generate inaccurate spurs, which are not encountered anatomically. Finally, we also investigated
 312 CAVnet's performance across multiple diseases (including a spectrum of DR severity) and healthy eyes,
 313 and across multiple devices. Our results indicate that CAVnet's performance was resilient to these
 314 different contexts.

315 Caliber and tortuosity are both important quantitative indicators of diabetes mellitus, cardiovascular
 316 disease, hypertension, and atherosclerosis³⁷⁻⁴²; however, because artery/vein differentiation is not usually
 317 performed in OCTA images, these quantities are usually not calculated separately for the different vessel
 318 types in OCTA imaging. However, our results indicate that pathophysiologic differences between these
 319 vessel types in disease are detectable by OCTA. Compared to eyes without DR (either healthy or diabetes
 320 mellitus without DR), the caliber of arteries is significantly reduced in eyes with either severe NPDR or
 321 PDR. We found that the caliber of veins is also reduced in the macular area, relative to eyes without DR.
 322 The reason may be that the basal membrane of arteries and veins in DR cases is thicker than in healthy
 323 controls; consequently, the functional vascular lumen is imaged by OCTA is smaller, with greater
 324 changes in arteries than in veins^{37,43}. Similarly, compared to healthy eyes, the arterial and venous caliber
 325 of eyes with BRVO significantly decreased in the central macula. As a previous study has demonstrated, a
 326 decrease in retinal arterial and venous diameters was seen in eyes with BRVO³¹. We could also detect
 327 variation in vessel caliber based on region. In healthy eyes, the caliber of veins ($82.6 \pm 31.0 \mu\text{m}$) is much
 328 larger than that of arteries ($69.6 \pm 25.3 \mu\text{m}$) at the nasal location ($P=0.003$). There is also a detectable
 329 difference in arterial ($48.2 \pm 2.2 \mu\text{m}$) and venous ($51.3 \pm 3.5 \mu\text{m}$) caliber in the temporal area ($P=0.006$). At
 330 the macula, however, there was no significant difference in artery and vein caliber. In the macula, we
 331 would expect differences between artery and vein caliber to diminish, as the size of the higher-order
 332 vessels prevalent in this region approaches the capillary limit. In addition, we also calculated the caliber
 333 of major vessels at the nasal location in healthy eyes. The mean caliber of the major veins (113.7 ± 20.2
 334 μm) is much larger than that of the largest arteries ($100.2 \pm 16.1 \mu\text{m}$) at the nasal location ($P=0.001$); these
 335 findings are similar to histological results²⁸. These results on healthy eyes can be taken as a further
 336 indication of the validity of CAVnet's output, since they concur with known retinal vascular physiology.

337 Unlike vessel caliber, our network's output produces arteries with tortuosity that is not significantly
 338 different than veins in healthy eyes. This result, and the tortuosity values we measure, are similar to a
 339 prior study^{29,44}. The arterial or venous tortuosity of eyes with DR has no great difference compared to that
 340 of eyes without DR. The lack of difference in tortuosity could be a result of large inherent variation in the
 341 population. The tortuosity of veins significantly increased in eyes with BRVO compared to healthy eyes,
 342 which is in line with clinical observations⁴⁵.

343 There are some limitations in CAVnet. First, CAVnet may generate false segmentation in some
 344 specific conditions. For example, CAVnet may misclassify part of an artery to a vein or vice versa, which
 345 may be because CAVnet over-learned the 'artery-vein-alternation rule' or over-relied on the conspicuous
 346 capillary-free zone near arteries (which could be mimicked by shadow artifacts). Similarly, the sensitivity
 347 for arteries is slightly higher than that of veins due to the same obviously capillary-free zone near the

348 retinal arteries in OCTA images, which would enable vessels to be more readily distinguished from the
 349 background. We were also unable to obtain helpful interpretable results within the 2-mm diameter circle
 350 centered on the optic disc because this area includes intricate vessel morphologies very different to the
 351 rest of the retina. In this region CAVnet had lower classification performance (sensitivity, $73.9\% \pm 12.2\%$;
 352 F1-score, $80.5\% \pm 10.1\%$; IoU, $68.5\% \pm 12.9\%$) than other areas. CAVnet generates incorrect artery-vein
 353 intersection segmentations at a higher rate than vein or artery mis-segmentations. This may be caused by
 354 the small number of samples of intersections in the training set. Furthermore, compared to arteries and
 355 veins, the number of pixels in an intersection is small even after the dilation we applied to the output. This
 356 means that a single misplaced pixel can lead to a large deterioration in performance metrics since it will
 357 represent a greater part of the sample. This is especially apparent in the IoU metric, which tends to
 358 penalize individual classification errors more than the F1-score (similar to L1 vs. L2 loss). We think that
 359 these facts probably largely explain the performance decline for intersection points. However, it should be
 360 noted that even though these performance metrics were less satisfactory, they largely represent clinically
 361 irrelevant, small differences in the location of a small number of pixels.

362 **5. Conclusion**

363 We proposed an end-to-end convolutional neural network that classifies arteries and veins: CAVnet.
 364 CAVnet not only classified arteries and veins down to the level of precapillary arterioles and postcapillary
 365 venules, but also detected the intersection of arteries (or arterioles) and veins (or venules). CAVnet has a
 366 high performance for differentiating arteries and veins, even in severe DR and BRVO cases.
 367 Measurements of arterial and venous caliber or tortuosity can potentially help with the diagnosis of DR
 368 and BRVO; our method is capable of extracting these measurements with high accuracy. Finally, CAVnet
 369 also performs well on wide-field images, an important capability in OCTA as bleeding edge research
 370 continues to push toward larger fields of view. We believe that this method can have applications in both
 371 the clinic and basic research.

372 **Funding**

373 National Institutes of Health (R01 EY027833, R01 EY024544, R01 EY031394, P30 EY010572, T32
 374 EY023211); unrestricted departmental funding grant and William & Mary Greve Special Scholar Award
 375 from Research to Prevent Blindness (New York, NY); Bright Focus Foundation (G2020168).

376 **Disclosures**

377 **Min Gao**, None; **Yukun Guo**, None; **Tristan T. Hormel**, None; **Kotaro Tsuboi**, None; **George
 378 Pacheco**, None; **David Poole**, None; **Steven T. Bailey**, None; **Christina J. Flaxel**, None; **David Huang**,
 379 Optovue (F, I, C, P); **Thomas S. Hwang**, None; **Yali Jia**, Optovue (F, P), Optos (P)

380 **Reference**

- 381 1. Jia Y, Tan O, Tokayer J, et al. Split-spectrum amplitude-decorrelation angiography with optical
382 coherence tomography. *Optics Express* 2012;20:4710–4725.
- 383 2. Jia Y, Baileya ST, Hwanga TS, et al. Quantitative optical coherence tomography angiography of
384 vascular abnormalities in the living human eye. *Proceedings of the National Academy of Sciences of the
385 United States of America* 2015;112:E2395–E2402.
- 386 3. Guo Y, Camino A, Wang J, et al. MEDnet, a neural network for automated detection of avascular area
387 in OCT angiography. *Biomedical Optics Express* 2018;9:5147–5158.
- 388 4. Guo Y, Hormel TT, Xiong H, et al. Development and validation of a deep learning algorithm for
389 distinguishing the nonperfusion area from signal reduction artifacts on OCT angiography. *Biomedical
390 Optics Express* 2019;10:3257–3268.
- 391 5. Wang J, Hormel TT, You Q, et al. Robust non-perfusion area detection in three retinal plexuses using
392 convolutional neural network in OCT angiography. *Biomedical Optics Express* 2020;11:330–345.
- 393 6. Guo Y, Hormel TT, Gao L, et al. Quantification of Nonperfusion Area in Montaged Widefield OCT
394 Angiography Using Deep Learning in Diabetic Retinopathy. *Ophthalmology Science* 2021;1:100027.
- 395 7. Wang J, Hormel TT, Gao L, et al. Automated diagnosis and segmentation of choroidal
396 neovascularization in OCT angiography using deep learning. *Biomedical Optics Express* 2020;11:927–
397 944.
- 398 8. Sharrett AR, Hubbard LD, Cooper LS, et al. Retinal arteriolar diameters and elevated blood pressure:
399 the atherosclerosis risk in communities study. *American Journal of Epidemiology* 1999;150:263–270.
- 400 9. Mitchell P, Cheung N, De Haseth K, et al. Blood pressure and retinal arteriolar narrowing in children.
401 *Hypertension* 2007;49:1156–1162.
- 402 10. Viswanath K, McGavin DDM. Diabetic retinopathy: clinical findings and management. *Community
403 eye health* 2003;16:21–4.
- 404 11. Hayreh SS, Zimmerman B, McCarthy MJ, Podhajsky P. Systemic diseases associated with various
405 types of retinal vein occlusion. *American Journal of Ophthalmology* 2001;131:61–77.
- 406 12. Samara WA, Shahlaee A, Sridhar J, et al. Quantitative optical coherence tomography angiography
407 features and visual function in eyes with branch retinal vein occlusion. *American Journal of
408 Ophthalmology* 2016;166:76–83.
- 409 13. Alam M, Toslak D, Lim JI, Yao X. Color fundus image guided artery-vein differentiation in optical
410 coherence tomography angiography. *Investigative Ophthalmology and Visual Science* 2018;59:4953–
411 4962.
- 412 14. Alam M, Toslak D, Lim JI, Yao X. OCT feature analysis guided artery-vein differentiation in OCTA.
413 *Biomedical Optics Express* 2019;10:2055–2066.
- 414 15. Xu X, Yannuzzi NA, Fernández-Avellaneda P, et al. Differentiating veins from arteries on optical
415 coherence tomography angiography by identifying deep capillary plexus vortices. *American Journal of
416 Ophthalmology* 2019;207:363–372.
- 417 16. Ishibazawa A, Mehta N, Sorour O, et al. Accuracy and reliability in differentiating retinal arteries and
418 veins using widefield en face OCT angiography. *Translational Vision Science & Technology* 2019;8:60–
419 60.

- 420 17. Kim T-H, Le D, Son T, Yao X. Vascular morphology and blood flow signatures for differential
421 artery-vein analysis in optical coherence tomography of the retina. Biomedical Optics Express
422 2021;12:367–379.
- 423 18. Hormel TT, Huang D, Jia Y. Artifacts and artifact removal in optical coherence tomographic
424 angiography. Quantitative Imaging in Medicine and Surgery 2021;11:1120–1133.
- 425 19. Alam M, Le D, Son T, et al. AV-Net: deep learning for fully automated artery-vein classification in
426 optical coherence tomography angiography. Biomedical Optics Express 2020;11:5249–5257.
- 427 20. Guo Y, Camino A, Zhang M, et al. Automated segmentation of retinal layer boundaries and capillary
428 plexuses in wide-field optical coherence tomographic angiography. Biomedical Optics Express
429 2018;9:4429–4442.
- 430 21. Gao M, Guo Y, Hormel TT, et al. Reconstruction of high-resolution 6×6-mm OCT angiograms using
431 deep learning. Biomedical Optics Express 2020;11:3585–3600.
- 432 22. Kondermann C, Kondermann D, Yan M. Blood vessel classification into arteries and veins in retinal
433 images. In: Pluim JPW, Reinhardt JM, eds. *Medical Imaging 2007: Image Processing*. Vol 6512. SPIE;
434 2007:651247.
- 435 23. Muraoka Y, Uji A, Ishikura M, et al. Segmentation of the four-layered retinal vasculature using high-
436 resolution optical coherence tomography angiography reveals the microcirculation unit. Investigative
437 Ophthalmology and Visual Science 2018;59:5847–5853.
- 438 24. Balaratnasingam C, An D, Sakurada Y, et al. Comparisons between histology and optical coherence
439 tomography angiography of the periarterial capillary-free zone. American Journal of Ophthalmology
440 2018;189:55–64.
- 441 25. Ghosh A, Kumar H, Sastry PS. Robust Loss Functions under Label Noise for Deep Neural Networks.
442 In: *31st AAAI Conference on Artificial Intelligence, AAAI 2017*. AAAI press; 2017:1919–1925.
- 443 26. Jadon S. A survey of loss functions for semantic segmentation. In: *2020 IEEE Conference on
444 Computational Intelligence in Bioinformatics and Computational Biology (CIBCB)*. IEEE; 2020:1–7.
- 445 27. Kingma DP, Ba JL. Adam: A method for stochastic optimization. In: *3rd International Conference on
446 Learning Representations, ICLR 2015 - Conference Track Proceedings*; 2015:1–15.
- 447 28. Ghasemi Falavarjani K, Al-Sheikh M, Darvizeh F, et al. Retinal vessel calibre measurements by
448 optical coherence tomography angiography. British Journal of Ophthalmology 2017;101:989–992.
- 449 29. Khansari MM, Garvey SL, Farzad S, et al. Relationship between retinal vessel tortuosity and
450 oxygenation in sickle cell retinopathy. International Journal of Retina and Vitreous 2019;5:1–7.
- 451 30. Kolar P. Risk factors for central and branch retinal vein occlusion: A meta-analysis of published
452 clinical data. Journal of Ophthalmology 2014;2014.
- 453 31. Youm DJ, Ha MM, Chang Y, Song SJ. Retinal Vessel Caliber and Risk Factors for Branch Retinal
454 Vein Occlusion. Current Eye Research 2012;37:334–338.
- 455 32. Adhi M, Filho MAB, Louzada RN, et al. Retinal Capillary Network and Foveal Avascular Zone in
456 Eyes with Vein Occlusion and Fellow Eyes Analyzed With Optical Coherence Tomography Angiography.
457 Investigative Ophthalmology & Visual Science 2016;57:OCT486–OCT494.
- 458 33. Ronneberger O, Fischer P, Brox T. U-Net: Convolutional Networks for Biomedical Image
459 Segmentation. In: *Medical Image Computing and Computer-Assisted Intervention – MICCAI 2015.
460 Lecture Notes in Computer Science()*. Vol 9351. Springer Verlag; 2015:234–241.

- 461 34. Ibtehaz N, Rahman MS. MultiResUNet : Rethinking the U-Net architecture for multimodal
462 biomedical image segmentation. *Neural Networks* 2020;121:74–87.
- 463 35. Son T, Alam M, Kim T-H, et al. Near infrared oximetry-guided artery–vein classification in optical
464 coherence tomography angiography: Experimental Biology and Medicine 2019;244:813–818.
- 465 36. Yang J, Yuan M, Wang E, Chen Y. Comparison of the Repeatability of Macular Vascular Density
466 Measurements Using Four Optical Coherence Tomography Angiography Systems. *Journal of*
467 *Ophthalmology* 2019;2019:1–7.
- 468 37. Stitt, A. W., Anderson, H. R., Gardiner, T. A., & Archer DB. Diabetic retinopathy: quantitative
469 variation in capillary basement membrane thickening in arterial or venous environments. *British Journal*
470 *of Ophthalmology* 1994;78:133–137.
- 471 38. Klein R, Sharrett AR, Klein BEK, et al. Are retinal arteriolar abnormalities related to atherosclerosis?
472 The atherosclerosis risk in communities study. *Arteriosclerosis, Thrombosis, and Vascular Biology*
473 2000;20:1644–1650.
- 474 39. Gepstein R, Rosman Y, Rechtman E, et al. Association of retinal microvascular caliber with blood
475 pressure levels. *Blood Pressure* 2012;21:191–196.
- 476 40. Kalitzeos AA, Lip GYH, Heitmar R. Retinal vessel tortuosity measures and their applications.
477 *Experimental Eye Research* 2013;106:40–46.
- 478 41. Stitt AW, Curtis TM, Chen M, et al. The progress in understanding and treatment of diabetic
479 retinopathy. *Progress in Retinal and Eye Research* 2016;51:156–186.
- 480 42. Heitmar R, Lip GYH, Ryder RE, Blann AD. Retinal vessel diameters and reactivity in diabetes
481 mellitus and/or cardiovascular disease. *Cardiovascular Diabetology* 2017;16:1–10.
- 482 43. Arichika S, Uji A, Murakami T, et al. Correlation of retinal arterial wall thickness with atherosclerosis
483 predictors in type 2 diabetes without clinical retinopathy. *British Journal of Ophthalmology* 2017;101:69–
484 74.
- 485 44. Saraf SS, Tyring AJ, Chen CL, et al. Familial retinal arteriolar tortuosity and quantification of
486 vascular tortuosity using swept-source optical coherence tomography angiography. *American Journal of*
487 *Ophthalmology Case Reports* 2019;14:74–78.
- 488 45. Wong TY, Scott IU. Retinal-Vein Occlusion. *New England Journal of Medicine* 2010;363:2135–2144.
- 489

490 **Figure legends**

491 Figure 1. CAVnet architecture. (A) is the input, consisting of an OCT angiogram of the inner retina. CAVnet has a
 492 U-net-like structure. The different colored rectangles represent operations with different parameters. The stride is
 493 represented by s. The dilation of the atrous convolutional layer is represented by r. The segmentation results output
 494 by CAVnet distinguishes between arteries and veins (B).

495 Figure 2. Ground truth generation. (A) Three angiograms of separate regions (nasal, macular, and temporal)
 496 montaged to produce a wide-field image. (B) The enhanced angiograms with low noise intensity, good connectivity,
 497 and strong contrast. (C) The manually delineated ground truth. Arteries are colored in red, green represents veins,
 498 and blue is intersection points. (D) Optic disc and (E) macular fundus photographs corresponding to OCTA, with
 499 arteries and veins indicated by red and green arrows. The original *en face* images of OCTA and fundus photographs
 500 serve as guides to delineate the accurate ground truth.

501 Figure 3. The performance of CAVnet classification demonstrated by a healthy eye (A1-A3) and an eye with severe
 502 proliferative diabetic retinopathy (PDR) (B1-B3). Row 1: retina angiograms montaged by nasal, macular and
 503 temporal scans. Row 2: ground truth of classification of arteries and veins. Row 3: prediction from CAVnet.

504 Figure 4. Examples of misclassification. (A, C) the input of CAVnet. (B, D) the segmentation results produced by
 505 CAVnet. The yellow arrows show segmentation errors in the output images. Mis-segmentation may be caused when
 506 CAVnet overfits the ‘artery-vein-alternation rule’ or when the capillary-free zone near arteries is unobvious. Artery-
 507 vein crossings may also make the algorithm generate misclassifications, however note that in most places the
 508 algorithm correctly interpreted crossing vessels.

509 Figure 5. Caliber map of the montaged wide-field angiograms from a diabetic eye without DR (A), an eye with mild
 510 to moderate NPDR (B), and an eye with severe PDR (C); boxplots of arterial (D) and venous (E) caliber compared
 511 between three groups at three scan locations. Kruskal-Wallis test (P^1) was first applied to suggest if there is a
 512 difference between at least one pair of groups, then a post-hoc test with Bonferroni correction (P^2) was applied to
 513 multiple pairs comparison.

514 Figure 6. Comparison of caliber between arteries and veins in healthy eyes. (A) Caliber map from a healthy eye. (B)
 515 Boxplot showing artery and vein caliber at three locations in healthy eyes. A Mann-Whitney U test (P^3) was applied
 516 to compare if there is a difference between artery and vein caliber at three locations.

517 Figure 7. Measurements of arterial and venous caliber at the nasal location. (A, B) The caliber (μm) of arteries and
 518 veins was measured in the ring area with a diameter of 1.7 mm to 3.4 mm centered on the optic disc (yellow circles).
 519 The cyan values indicate the caliber of the veins. The yellow values represent the caliber of arteries.

520 Figure 8. Tortuosity map of the montaged wide-field angiograms from a diabetic eye without DR (A), an eye with
 521 mild to moderate NPDR (B), and an eye with severe PDR (C). Brighter colors (green arrows) indicate the higher
 522 tortuosity of the vessel. (D, E) Comparison of tortuosity between eyes without DR and eyes with DR. No significant
 523 difference in mean tortuosity of eyes with DR compared to eyes without DR was found, as evaluated by the
 524 Kruskal-Wallis test (P^1).

525 Figure 9. (A) Tortuosity map from a healthy eye. (B) Comparison of mean tortuosity between arteries and veins in
 526 healthy eyes. There is no significant difference between arterial and venous tortuosity in healthy eyes, as evaluated
 527 by the Mann-Whitney U test (P^3).

528 Fig 10. CAVnet output in an eye with BRVO (top row) and a healthy control (bottom row). (A) macular angiograms.
 529 (B) CAVnet output for (A). (C) Vessel caliber map. (D) Tortuosity map. The prediction showed high accuracy on
 530 scans from eyes with branch retinal vein occlusion (BRVO). The changes in arterial and venous caliber can be
 531 observed in the caliber map. The high tortuosity of veins in BRVO is obvious in the tortuosity map.

532 Figure 11. Comparison of the mean arterial and venous caliber and tortuosity of 17 healthy eyes and 64 eyes with
 533 BRVO in the macular center area. (A) Comparison of caliber. (B) Comparison of tortuosity. A Mann-Whitney U test
 534 (P^3) was used to compare whether caliber and tortuosity deviate significantly from a healthy distribution in BRVO
 535 eyes. Compared to healthy eyes, the caliber of arteries and veins both greatly reduced in eyes with BRVO. The
 536 tortuosity of veins significantly increased.

537 Figure 12. CAVnet outputs for larger-field-of-view scans. (A) 9×9-mm angiogram of the retina.
538 (B) Ground truth.
(C) predicted result by CAVnet for A. The results show high accuracy on 9×9-mm scans.

Table 1. Datasets.

Dataset for convolutional network					
	Disease	Nasal	Macula	Temporal	Eyes
Training dataset	No DR	Healthy control	10	10	10
		Diabetes without DR	19	19	19
	DR	Mild to moderate NPDR	27	22	27
		Severe NPDR or PDR	32	28	32
Test dataset	No DR	Healthy control	17	17	17
		Diabetes without DR	8	8	8
	DR	Mild to moderate NPDR	25	25	25
		Severe NPDR or PDR	25	25	25
BRVO dataset					
	Disease	Scans		Eyes	
	BRVO	64		64	
9×9-mm scans from Solix					
	Disease	Scans		Eyes	
	Healthy control	13		5	

Table 2. Artery and vein segmentation performance on test dataset (N of scan=225).

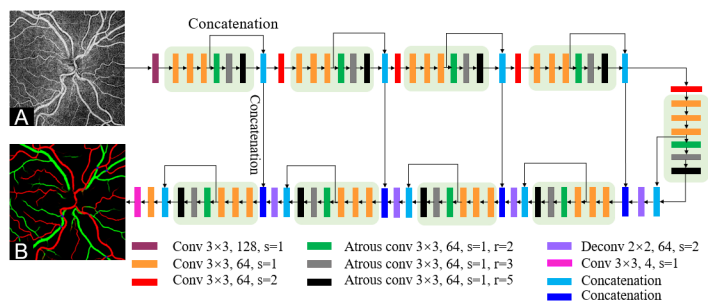
	Sensitivity (%)	Specificity (%)	F1-score (%)	IoU (%)
Artery	95.3±4.1	99.6±0.3	94.2±4.1	89.3±7.0
Vein	94.4±5.0	99.7±0.3	94.1±4.3	89.2±7.2
Intersection points	76.3±18.6	1.0±0.0	85.2±13.2	76.3±18.6

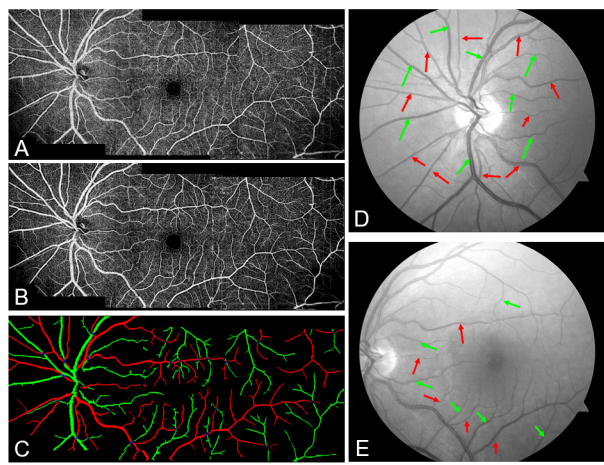
Table 3. Artery and vein segmentation performance on eyes diagnosed with branch retinal vein occlusion (N of scan =64).

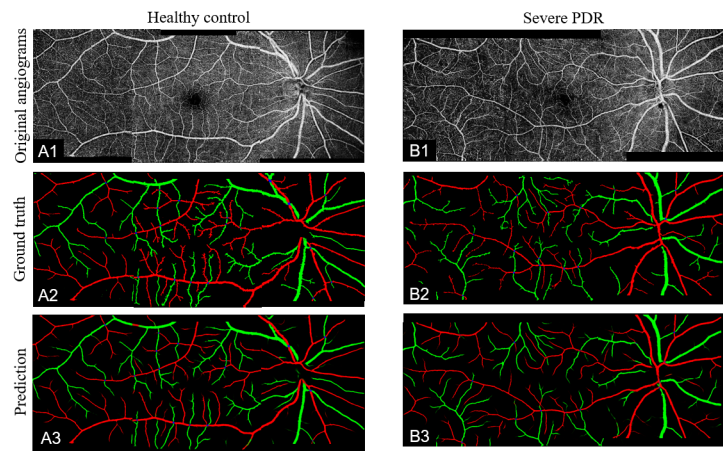
	Sensitivity (%)	Specificity (%)	F1-score (%)	IoU (%)
Artery	97.4±2.7	99.6±6.0	94.5±3.6	89.9±6.4
Vein	92.2±0.1	99.9±0.1	94.6±3.8	90.0±6.6
Intersection points	93.7±8.9	1.0±0.0	96.5±5.2	93.7±8.9

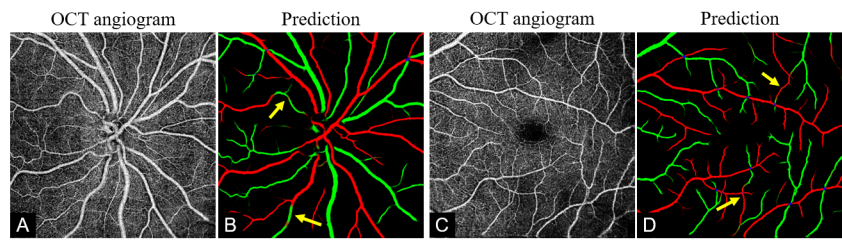
Table 4. Artery and vein segmentation performance on 9×9-mm scans from Solix (N of scan =13).

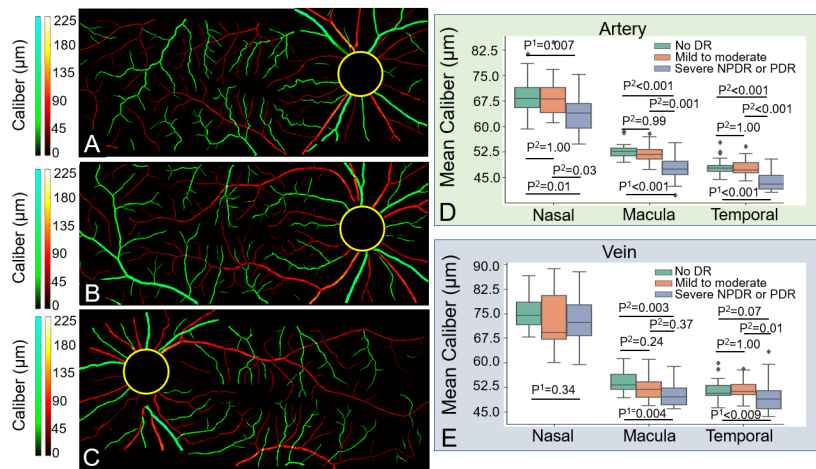
	Sensitivity (%)	Specificity (%)	F1-score (%)	IoU (%)
Artery	91.3±0.2	99.7±0.2	92.6±2.2	86.4±3.7
Vein	87.0±4.0	99.9±0.0	92.1±2.4	85.5±4.0
Intersection points	91.0±10.2	1.0±0.0	94.9±6.1	91.0±10.2

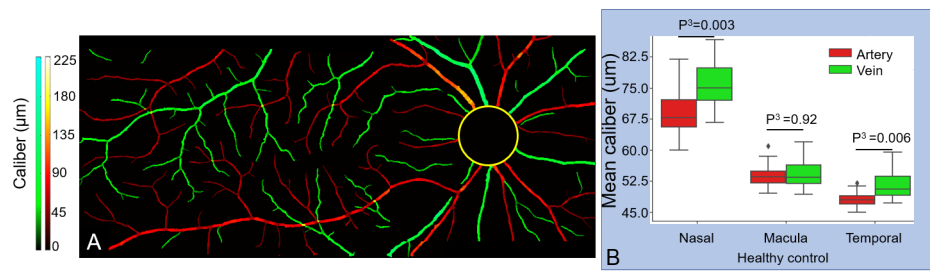


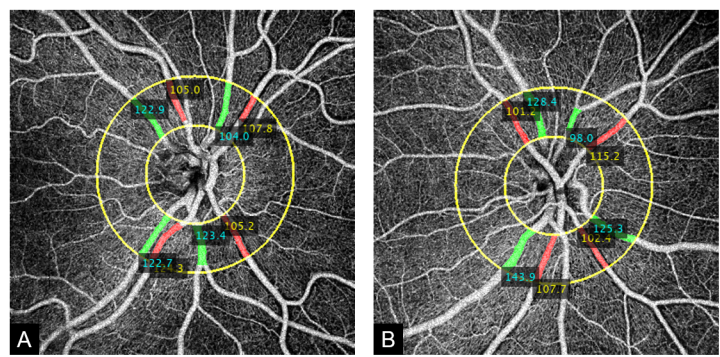


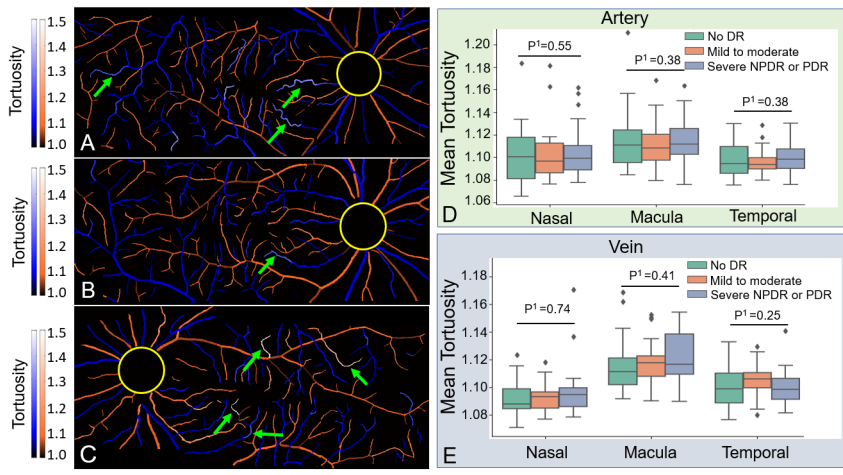


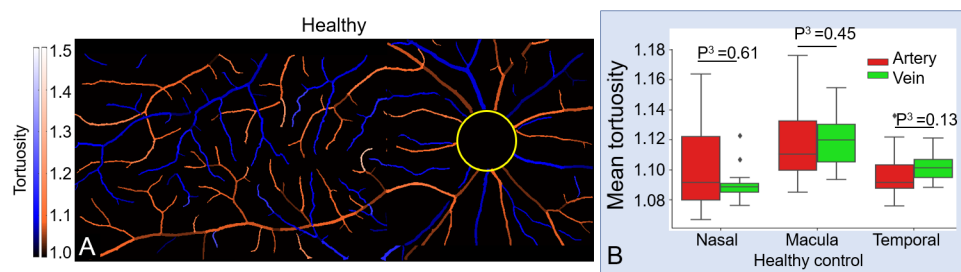


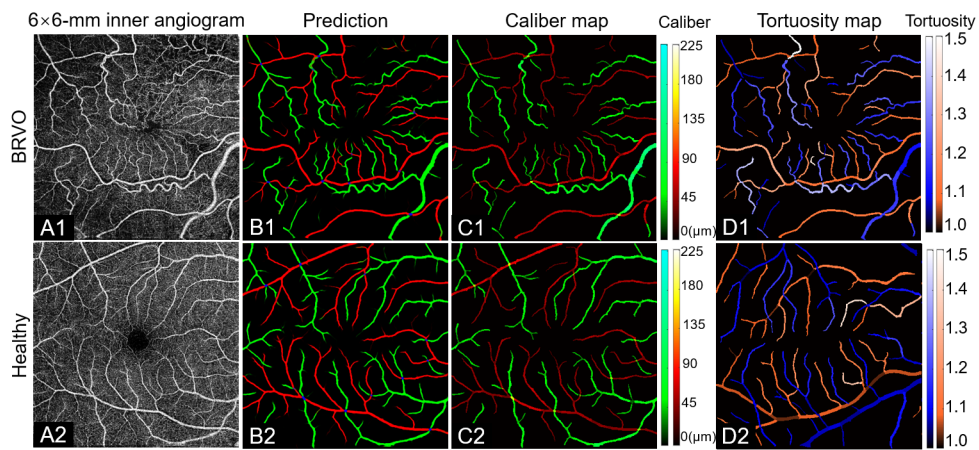


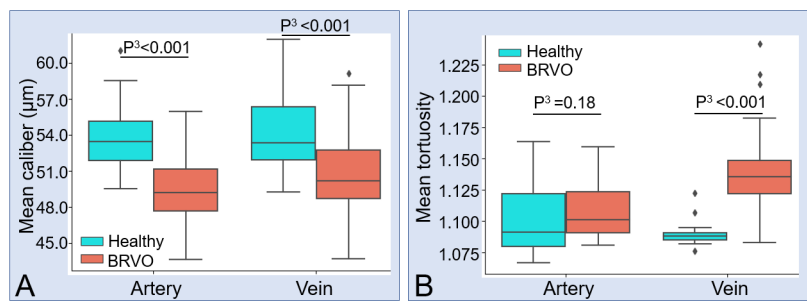


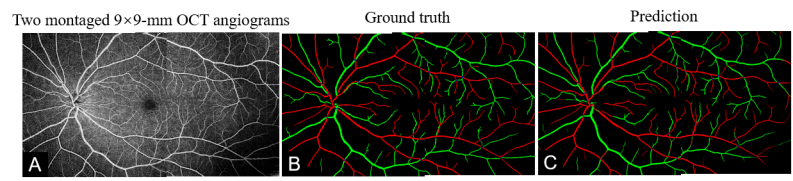












Précis

A deep learning network was developed to classify arteries and veins in montaged wide-field OCT angiograms, which is potentially useful in the analysis of vessel type-specific features on diseases.